communications earth & environment

Article

A Nature Portfolio journal

https://doi.org/10.1038/s43247-025-03034-1

Airborne blue lidar reveals the ocean's hidden biological engine in the South China Sea

Check for updates

Chen Peng [1,2,10] ✉, Cédric Jamet [3], Paolo Di Girolamo[4], Davide Dionisi [5], Xinye Li[1], Siqi Zhang [1,2,10], Zhenhua Zhang [1,2,10], Weibiao Chen[6,7,8] ✉, Yan He[6,7,8] ✉, Kun Shi [9] ✉ & Delu Pan[1,2]

The ocean's biological carbon pump, a critical climate regulator, is driven by phytoplankton ecosystems hidden from satellites. This observational blind spot has left the dynamics of the crucial subsurface chlorophyll maximum layer—a key engine of ocean productivity—unquantified across large scales. Here, we address this limitation with an airborne blue lidar system, engineered with a deep-penetrating blue laser (486 nm) and a hybrid detector to achieve extended profiling depth and dynamic range. During campaigns in the South China Sea, our validated system produced continuous, high-resolution profiles of chlorophyll architecture down to 100 meters, nearly doubling the reach of existing lidar technology. This capability provides a direct means to quantify the spatial heterogeneity of subsurface chlorophyll maximum layers, shifting the characterization of the ocean's carbon cycle from an inferred picture to a directly observed reality. Our work provides a technological basis for next-generation of space-based missions to monitor the ocean's interior.

Global climate models, our primary tools for predicting Earth's future, remain limited by a key uncertainty: the dynamics of the ocean's biological carbon pump[1–3]. A vast, hidden engine of phytoplankton ecosystems, the Subsurface Chlorophyll Maximum (SCM), operates beyond the view of satellites, leaving a critical gap in our ability to accurately model ocean productivity and carbon sequestration[4–6]. This observational gap in the ocean's interior means that a fraction of the global carbon cycle is poorly constrained, potentially leading to systematic biases in climate projections[7–10]. For decades, the immense contribution of these subsurface ecosystems has been inferred rather than measured, representing one of the most significant and persistent challenges in Earth system science.

This blind spot exists because our current observational toolkit is not fully adequate for this task. Traditional ship-based observations, while invaluable for discovering large-scale variations such as high-nutrient, low-chlorophyll zones[11,12], suffer from inherent drawbacks because of their sparse spatial and temporal coverage, prohibitive cost, and bias toward summer-season sampling due to weather constraints[13]. On the other hand, satellite ocean color sensors, which have provided extensive global coverage and continuous records since the late 1970s[14], are fundamentally restricted to the top few meters of the surface[15]. The efficacy of these methods is further compromised by cloud cover, sun glint, and atmospheric interference, leading to data gaps that often exceed 70% in daily global products[16]. Similarly, while in situ biogeochemical profiling floats provide valuable depth-resolved chlorophyll-*a* data, they are also constrained by sparse spatial distributions, preprogrammed surfacing intervals, and high deployment costs, limiting their capacity to capture fine-scale spatio-temporal variability and achieve comprehensive regional monitoring[13,17].

Even airborne lidar, a promising technology for vertical profiling, has been hampered by two significant challenges. Airborne systems using green lasers (e.g., 532 nm) have been demonstrated to monitor ocean optical properties[15,16,18–27] and have shown value in estimating primary production and carbon export[28–31]. However, their effective profiling depth is

[1]State Key Laboratory of Satellite Ocean Environment Dynamics, Second Institute of Oceanography, Ministry of Natural Resources, Hangzhou, China. [2]Southern Marine Science and Engineering Guangdong Laboratory (Guangzhou), Guangzhou, China. [3]Université Littoral Côte d'Opale, CNRS, Université Lille, IRD, UMR 8187, Laboratoire d'Océanologie et de Géosciences (LOG), Wimereux, France. [4]Università della Basilicata, Potenza, Italy. [5]Institute of Marine Sciences (ISMAR), Italian National Research Council (CNR), Rome, Tor Vergata, Italy. [6]Wangzhijiang Innovation Center for Laser, Aerospace Laser Technology and System Department, Shanghai Institute of Optics and Fine Mechanics, Chinese Academy of Sciences, Shanghai, China. [7]Shanghai Key Laboratory of All Solid-State Laser and Applied Techniques, Shanghai Institute of Optics and Fine Mechanics, Chinese Academy of Sciences, Shanghai, China. [8]Center of Materials Science and Optoelectronics Engineering, University of Chinese Academy of Sciences, Beijing, China. [9]Taihu Laboratory for Lake Ecosystem Research, State Key Laboratory of Lake Science and Environment, Nanjing Institute of Geography and Limnology, Chinese Academy of Sciences, Nanjing, China. [10]These authors contributed equally: Chen Peng, Siqi Zhang, Zhenhua Zhang. ✉e-mail: chenp@sio.org.cn; wbchen@siom.ac.cn; heyan@siom.ac.cn; kshi@niglas.ac.cn

fundamentally limited to less than 50 *m* because of the rapid attenuation of light in water[32]. More importantly, intense reflected light from the sea surface can easily saturate detectors, which not only contaminates the subsurface signal but also further curtails the penetration depth[33]. These sensor-specific constraints collectively define a technological gap: we lack a tool capable of rapid, continuous, and deep sea profiling of ocean biological structures, particularly within the crucial 0–100-meter range where subsurface chlorophyll maximum layers (SCMLs) reside.

To close this observational gap, we developed and deployed an airborne blue lidar system that addresses these limitations through three synergistic technical solutions. First, a custom-developed 486 *nm* blue laser matches the optimal transmission window of clear oceanic water, maximizing deep penetration. Second, a hybrid analog/photon-counting detector captures both the blind surface echo and the faint single-photon returns from depth, achieving an unprecedented dynamic range. Finally, an adaptive detection strategy effectively eliminates the sea surface glint effect to preserve the integrity of the subsurface signal. These integrated solutions enable continuous particle sampling from the sea surface down to 100 m corresponding to ~4.2 optical depths, or the ~1.8% of surface irradiance, in these clear waters, opening a window into the ocean's hidden biology.

Results and discussion

A lidar architecture to overcome fundamental barriers

To achieve the objective of profiling chlorophyll down to 100 m, our airborne lidar was designed to overcome three key challenges that have constrained previous systems: poor light penetration in water, an extensive signal dynamic range, and detectors' overloading sea reflections. We engineered a system with three synergistic solutions to address each of these problems. (Fig. 1).

First, to see deeper, we optimized the laser color. While conventional systems use green light (532 nm), which is suitable for turbid coastal zones, blue light penetrates far more effectively in the vast, clear open ocean[34]. We therefore developed a powerful and highly stable blue laser source operating at 486 nm, a wavelength tuned to the ocean's deep transmission window. This choice was important for maximizing the signal returned from significant depths.

Second, to capture the full range of light intensity, we designed a hybrid detector. The lidar signal attenuates exponentially in water, creating a dynamic range challenge of over five orders of magnitude: the return from the surface is intensely bright, whereas the signal from 100 m can be as faint as a single photon. Standard detectors are either sensitive enough for deep signals but are blinded by the surface or can handle the surface but lack the ability to see photons backscattered from depths greater than a few meters. Our solution is an innovative analog/photon-counting composite photoelectric detection (APCD) scheme. This system functions as two detectors in one, seamlessly combining analog detection for strong near-surface returns with highly sensitive single-photon counting for weak signals from depth, creating a single, continuous high-fidelity profile.

Finally, to isolate the true underwater signal, we eliminate surface glint. The intense flash of light reflected from the sea surface can easily contaminate adjacent subsurface data. We implemented an adaptive dual-gain sea surface glint rejection detection (DGD) strategy. This intelligent system

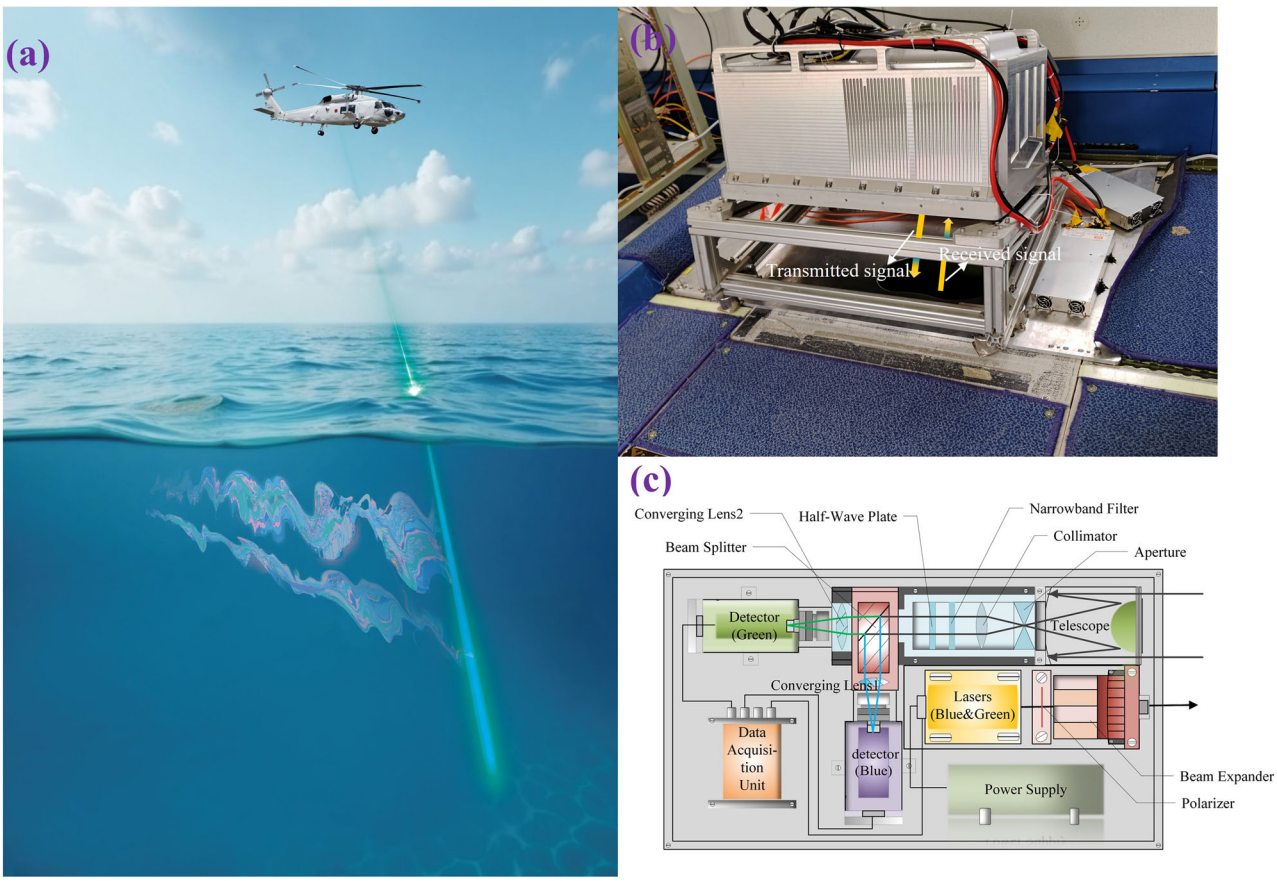

Fig. 1 | An airborne lidar system engineered to reveal the ocean's hidden biology. **a** Conceptual illustration of the system remotely profiling deep subsurface chlorophyll layers. **b** The instrument integrated on the research aircraft. **c** Schematic of the system architecture. The design's novelty lies in three synergistic components engineered to overcome fundamental observational barriers: a high-energy blue laser source (HEBLS) to solve the deep penetration challenge; an advanced analog/photon-counting composite photoelectric detection (APCD) module to manage an extensive signal dynamic range; and an adaptive dual-gain sea surface glint rejection detection (DGD) strategy to suppress corrupting surface reflections. Together, these innovations enable continuous retrieved chlorophyll-*a* profiling from the surface to 100 m. The key specifications are listed in Supplementary Table S1.

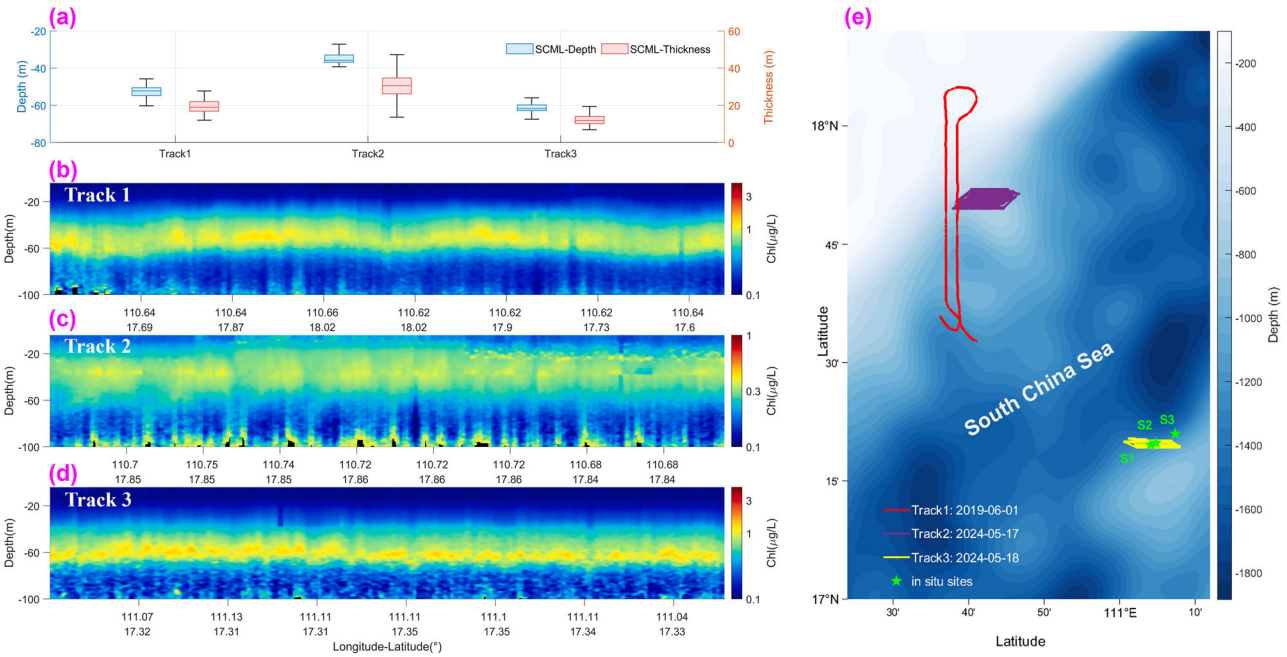

Fig. 2 | Lidar reveals the fine-scale architecture and spatial heterogeneity of the ocean's hidden phytoplankton layers. a Quantitative comparison of subsurface chlorophyll maximum layer (SCML) characteristics across three tracks, revealing variations in depth (blue boxes) and thickness (red boxes). The box plots indicate the median (center line), 25th and 75th percentiles (box edges), and the most extreme data points not considered outliers (whiskers). **b–d** Corresponding high-resolution retrieved chlorophyll-*a* curtains measured via airborne lidar along Track 1, Track 2, and Track 3. These profiles consistently resolve complex chlorophyll structures down to 100 m deep. **e** Map showing the flight paths in the South China Sea. In situ measurements at stations S1–S3 (green stars) were used for validation, and the validation stations S1–S3 are located on Track 3. Collectively, these panels provide the first continuous, large-scale visualization of the dramatic structural differences in a critical, yet previously hidden, component of the marine ecosystem.

effectively ignores brief, overwhelming surface reflection, preserving the integrity of crucial data from just below the surface down to greater depths. Together, these solutions create a system capable of profiling the ocean to greater depths.

Lidar mapping of the ocean's hidden vertical structure

Our blue lidar provided fresh insights into the ocean's biological architecture. Flying extensive transects across the South China Sea, our advanced lidar methods are able to resolve the fine-scale vertical structure of subsurface chlorophyll-a down to 100 m depth—a depth realm that has been inaccessible from traditional remote sensing techniques.

The data revealed the dynamism and heterogeneity of the SCMLs (Fig. 2). For example, along a single transect (Track 1), we observed a sharply defined SCML centered consistently at ~52 m with a 19 m thickness. In stark contrast, a nearby region surveyed years later (Track 2) exhibited a much more diffuse ecosystem, with lower overall chlorophyll concentrations and a shallower, broader SCML centered at 36 m and spanning over 30 m in thickness. Farther south (Track 3), the SCML plunged deeper to ~62 m and was compressed into a remarkably thin 12-m layer. The ability to resolve these fine-scale shifts in ecosystem structure across vast stretches of ocean represents an advance in oceanographic observations.

To rigorously validate these airborne maps, we conducted simultaneous in situ chlorophyll measurements at three strategic stations (S1–S3). The ground-truth data confirmed the exceptional accuracy and resolving power of our lidar in characterizing these hidden biogeochemical features. The scatter plots reflect the inherent challenges of validating high-resolution airborne data with ship-based point measurements. These include: (1) spatio-temporal mismatch errors between the high-speed aircraft and stationary ship measurements; (2) the inherent patchy distribution of marine phytoplankton at fine scales; and (3) regional variations in the bio-optical relationships used in the retrieval algorithm. These findings demonstrate the capability of our technique for advancing marine ecosystem monitoring.

Performance benchmark: blue and green lidars for ocean profiling

To quantify the performance advantage of our system, we conducted a direct, head-to-head comparison against a conventional green (532 nm) lidar with a standard linear-mode analog detector, an enhanced green lidar utilizing our advanced APCD + DGD technology, and a blue lidar, also with APCD + DGD detection. This design allows us to isolate the benefits of the optimal blue wavelength. The results establish the blue lidar's superior performance, demonstrating a improvement in deep-ocean profiling capability. (Fig. 3).

The physical basis for this leap is the blue laser's significantly deeper penetration in clear oceanic waters. This is illustrated in the signal-to-noise ratio (SNR) profiles, where our blue lidar maintains a robust signal (SNR ≥ 4) to ~110 m. This extends the effective range to nearly double that of the conventional green lidar (~55 m), which fails entirely to penetrate the deep chlorophyll maximum layer. Critically, even when enhanced with our advanced detector, the green lidar's reach is still fundamentally limited by the wavelength to ~88 m (Fig. 3).

This superior depth penetration translates directly into an enhanced capacity for ecosystem mapping. Our blue lidar successfully retrieved high-fidelity chlorophyll-*a* profiles across the entire 0–100-meter water column (corresponding to ~4.6 optical depths, or the 1% isolume, in these clear waters.), capturing the full vertical architecture of the phytoplankton community. In stark contrast, both green lidar systems were blind to the deeper parts of the ecosystem, failing to characterize the full extent and structure of the SCML.

Validation against simultaneous in situ measurements confirmed the quantitative accuracy of our lidar retrievals. The analysis shows that within the overlapping depth range detectable by both lidars (primarily the upper ocean), the performance of the enhanced green lidar is comparable to that of the blue lidar, while the conventional system struggled to produce reliable retrievals. However, this comprehensive benchmark reveals a fundamental

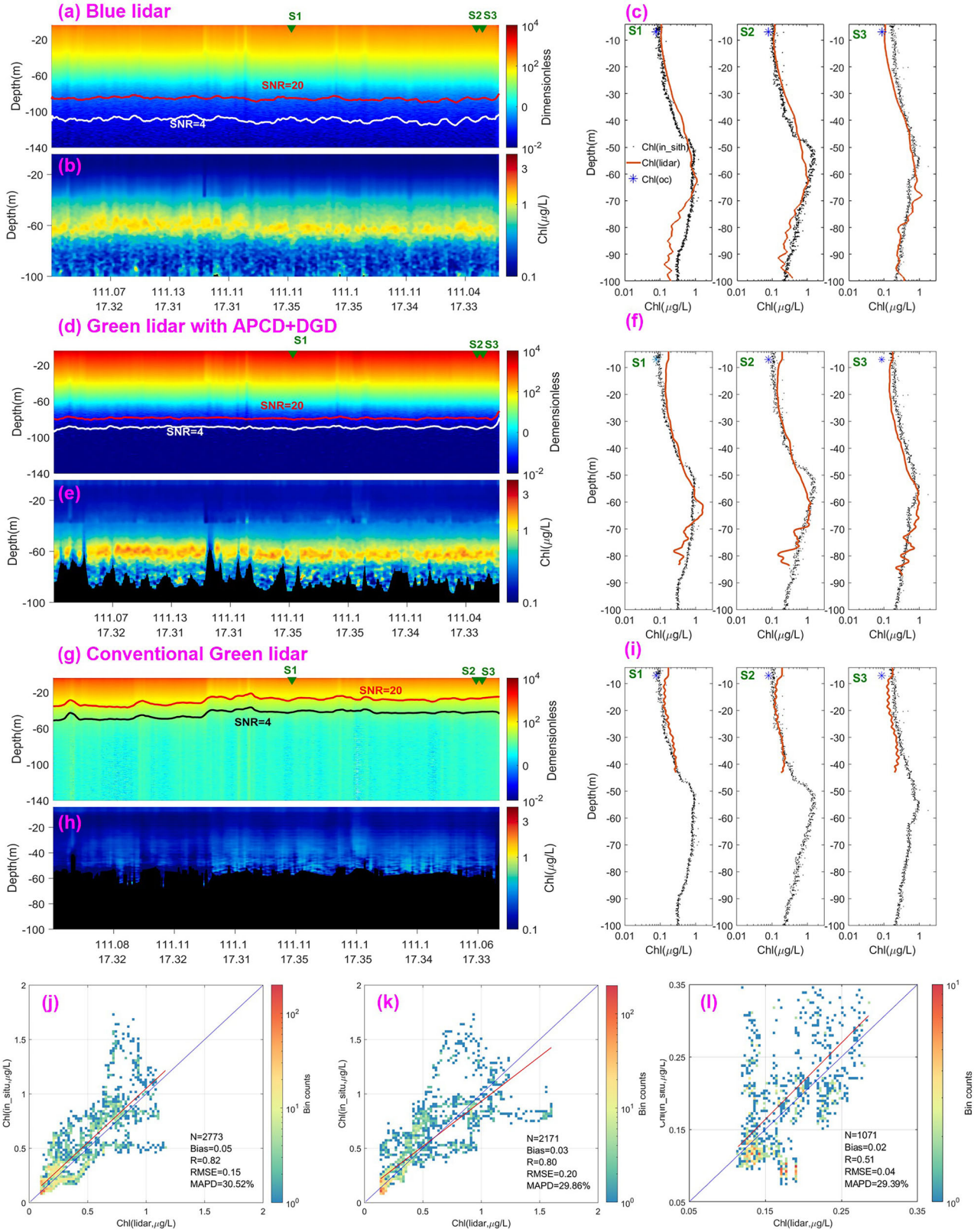

Fig. 3 | Head-to-head benchmark revealing the superior performance of the blue lidar. All panels correspond to data from Track 3. The S1, S2, and S3 profiles represent the average profiles derived from multiple CTD fluorometer casts at the corresponding stations, which are used for comparison with the lidar profiles. **a**, **d**, **g** Signal-to-noise ratio (SNR) curves for the blue lidar, an enhanced green lidar with APCD + DGD, and a conventional green lidar. The white/black lines indicate SNR thresholds, showing the blue lidar's dramatically deeper signal penetration. **b**, **e**, **h** Corresponding retrieved chlorophyll-*a* concentration profiles, demonstrating that only the blue lidar captures the full vertical ecosystem structure. **c**, **f**, **i** Comparison of lidar-retrieved profiles (orange lines) with simultaneous in situ measurements (black dots). **j**, **k**, **l** Scatter plots showing the blue lidar's higher correlation (*R*) and lower error (RMSE) against ground-truth data. Collectively, this benchmark demonstrates that the synergy of the optimal blue wavelength and advanced detection is essential for quantitatively accurate profiling of deep-ocean ecosystems.

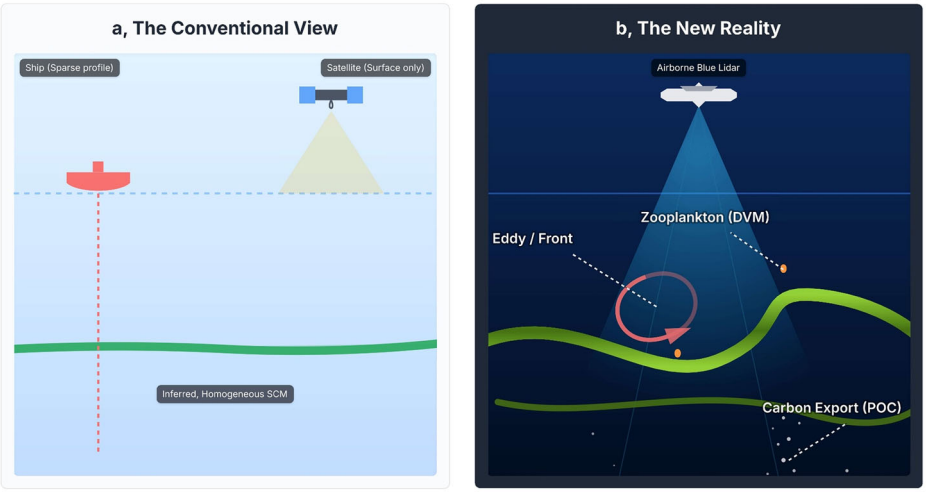

Fig. 4 | A new perspective on observing the ocean's biological engine. a The conventional view, based on satellite surface data and sparse ship-based profiles, depicted the Subsurface Chlorophyll Maximum (SCM) as a relatively simple, homogeneous layer, leaving key ecological processes unresolved. **b** Our airborne blue lidar provides the first continuous, high-resolution view, revealing the SCM's true nature as a highly complex and heterogeneous ecosystem. It quantitatively resolves fine-scale structures shaped by physical processes like eddies and fronts, and captures the biological context, including zooplankton migration (DVM) and subsequent carbon export (POC). This leap in observational capability is critical for accurately modeling marine productivity and the global carbon cycle.

difference that stems not from retrieval accuracy in the upper water column, but from the physical limits of penetration depth. As shown in Fig. 3, the signal from the enhanced green lidar attenuates completely at ~88 m, thus failing to capture the full structure of the deep chlorophyll maximum (SCM), especially its core and bottom regions. In contrast, the blue lidar penetrates to 110 m, completely resolving the entire vertical structure of the phytoplankton community in the 0–100 meter water column. Therefore, while the enhanced green lidar is a powerful tool for studying the upper ocean, our results demonstrate that for tasks requiring complete, quantitative profiling of the deep-ocean SCM, the blue lidar is the only technology of those tested capable of providing the necessary data. This capability is critical for accurately assessing marine ecosystems and conducting robust scientific modeling.

Implications and significance

The development of our airborne blue lidar system represents an important advance in ocean remote sensing, altering our ability to observe the ocean's interior from a sparse, inferred understanding to a direct, high-resolution view (Fig. 4). This technology provides an enhanced capability to profile chlorophyll-*a* continuously and at high resolution from the surface to more than 100 m, directly addressing a long-standing observational gap concerning the dynamics of SCMLs, which are fundamental to marine primary production, nutrient cycling, and the ocean's biological carbon pump[8,35,36]. Beyond improving existing models, our high-resolution observations challenge the foundational assumptions upon which many regional carbon export estimates are built. We reveal that the SCM is far more structurally heterogeneous and dynamic than previously assumed (Fig. 2). This finding implies that past calculations of carbon flux, which often relied on smoothed, spatially-averaged data from sparse profiles, may have underestimated or misinterpreted the true biological activity. For instance, thin, high-density filaments of phytoplankton, often associated with submesoscale eddies and fronts[4–6], invisible to coarse sampling but now resolvable by our lidar, could represent ephemeral hotspots of primary production and carbon export that were previously unaccounted for. Our work therefore suggests that a re-evaluation of carbon transport mechanisms in these key oceanic regions may be necessary, moving from a simplified, layered view to one that embraces fine-scale complexity.

Furthermore, the synchronous high-resolution optical profiles (Kd and bbp) provided by this technology open avenues for investigating the formation mechanisms of the SCM. It is traditionally understood that SCM formation results from a complex interplay of mechanisms, including the physical accumulation of biomass and the photoacclimative regulation of intracellular chlorophyll content[4–6]. By synergistically analyzing the fine structures of Kd, bbp, and chlorophyll-a profiles, future research may be able to better disentangle the relative contributions of these two mechanisms. For instance, a thin layer with synchronously enhanced bbp and chlorophyll-a would more likely represent true biomass accumulation, whereas a layer with a significant increase in chlorophyll-a but little change in bbp would likely indicate the dominance of photoacclimation[2,37,38]. This discriminative power, unavailable from any previous large-scale observational technique, will greatly deepen our understanding of how marine ecosystems respond to the physical environment.

To quantify the biogeochemical significance of resolving such fine-scale structures, we compared our high-resolution, lidar-derived profiles against a traditional modeling approach that assumes a Gaussian distribution for the vertical chlorophyll profile. We calculated the depth-integrated chlorophyll for both the directly measured profiles and the Gaussian-fitted models. The comparison yields a Mean Absolute Percentage Difference (MAPD) of 30–50% between the two methods (see Supplementary Fig. S1). Since primary production and subsequent carbon export are directly linked to this biomass, this suggests that failing to resolve such features in basin-scale models could introduce a systematic underestimation of subsurface biological carbon pools and their contribution to the carbon pump. This regional quantification provides tangible, first-order evidence of this observational bias, a bias our technology is now poised to correct.

While this study robustly validates the system's performance in the South China Sea, its applicability across diverse oceanic regimes is supported by extensive research. As shown in Supplementary Fig. S2, the clear, "Type 1" oligotrophic waters where our blue lidar excels—defined as having a diffuse attenuation coefficient K_d (490) ≤ 0.1 m^{-1}—constitute ~89% of the global ocean surface. This visual evidence underscores that our technology is not limited to a specific region but is optimally suited for the largest, yet most under-observed, biomes on Earth. Furthermore, the fine-scale structural heterogeneity of the SCM we observed is not a localized phenomenon but is understood to be a ubiquitous feature of the world's oceans. In the vast oligotrophic gyres of the Atlantic and Pacific, for instance, mesoscale eddies are known to modulate the nutricline depth, shaping the SCM and creating localized productivity hotspots that are critical for basin-scale biogeochemical budgets[39–41]. At even finer scales, submesoscale fronts and filaments are hypothesized to drive intense vertical nutrient fluxes, generating thin, high-density phytoplankton layers that contribute disproportionately to primary production and carbon export[42,43]. However, these physically-driven biological structures have largely eluded direct, large-scale observation. Previous understanding has been built primarily on numerical models[42,44] and sparse in-situ measurements[13,40], creating a long-standing gap between theoretical understanding and observational capacity.

Our system's ability to precisely map the vertical architecture of phytoplankton provides a valuable tool for oceanographic research. Previous studies have shown that, compared with satellite-only methods, resolving the vertical structure of phytoplankton can improve net primary production

estimates by up to 54%[45]. Our lidar enables refined characterization of particulate organic carbon (POC) export pathways, which is crucial, as a significant fraction of long-term carbon sequestration occurs via non-gravitational transport mechanisms[46,47] (e.g., migrating zooplankton[48,49], subduction of suspended particles[50]) that are intrinsically linked to the fine-scale biological structures now resolvable by our system. These data will significantly enhance the accuracy of ocean productivity models, leading to a more nuanced understanding of the ocean's role in global climate regulation[51,52]. Crucially, our chlorophyll retrievals, while refined by machine learning, are fundamentally constrained by the physically-derived optical properties (K_d and *bbp*), ensuring robust, interpretable results.

In an era of accelerating ocean warming, our blue lidar provides a useful tool for dissecting how marine ecosystems respond to climate stressors. While satellite records show complex, regionally varying chlorophyll trends—including declines in stratified gyres[4,8,9,53] and increases at high latitudes[36,54,55]—our technology can, for the first time, elucidate the mechanisms driving these depth-dependent phytoplankton responses, which often differ significantly from surface community changes[48]. Monitoring these shifts is vital for assessing the impacts on POC flux, the biological carbon pump, and long-term carbon storage[56]. Furthermore, these data can provide more accurate inputs for models seeking to understand the surface biological processes that can influence oxygen minimum zone (OMZ) variability, as OMZs can arise from stratified photosynthesis and vertical light attenuation[57]. As a potential future application, the high-resolution scattering profiles also offer the capability to detect layers associated with the diel vertical migration of zooplankton[46,47], which would improve estimates of biologically mediated vertical carbon flux, particularly active transport by zooplankton to the mesopelagic zone (the "migration pump")[50].

The ability to detect fine-scale ecosystem shifts offers the potential for early warning and improved tracking of marine habitat resilience to climate stressors[47]. For instance, subtle but persistent changes in the depth, thickness, or internal structure of the SCM may serve as precursors to larger, basin-scale regime shifts, providing an early warning of ecosystem stress long before changes are detectable at the surface. By quantifying how these subsurface structures respond to and recover from disturbances such as marine heatwaves, we can directly assess the resilience of the ocean's biological engine. This information is critical for understanding how changes in phytoplankton distributions affect marine biodiversity[58], food web structures[59], global fisheries[60], and overall ecosystem services[61]. By filling crucial observational voids in deep phytoplankton profiling, our blue lidar system has the potential to furnish previously unattainable data essential for improving the fidelity of global climate models. More accurate representations of subsurface phytoplankton distribution and productivity are paramount for refining predictions of ocean responses to environmental variability and long-term climate change, thereby informing robust conservation strategies and adaptive management plans for a rapidly changing ocean.

While this paper focuses on the advantages of blue lidar in the open ocean, the dual-wavelength capability of our system also offers potential for studying more productive waters. The concurrent 532 nm green laser channel is better suited for the more turbid, higher-chlorophyll waters of coastal and shelf seas, where blue light is more rapidly attenuated. This versatility greatly expands the system's range of applications, positioning it as a comprehensive observational platform capable of covering environments from the coast to the open ocean and addressing a wider array of biogeochemical questions. The dual-wavelength lidar system presented in this study opens possibilities for future ocean remote sensing. The synchronous acquisition of attenuation coefficients at different wavelengths (e.g., Kd(486) and Kd(532)) has the potential to provide additional information on the properties of suspended particles in the water column (such as size distribution and composition), thereby enabling a more precise distinction between SCMs caused by biomass accumulation versus photoacclimation. This multi-spectral capability will significantly enhance the accuracy of our retrievals for key parameters like chlorophyll and POC, representing a critical direction for the future development of airborne and spaceborne ocean lidars.

While airborne lidar systems, such as the one presented here, offer advancements in regional-scale ocean observations, achieving global, continuous monitoring of subsurface ocean dynamics necessitates the development and deployment of spaceborne ocean lidar systems. The success of our blue lidar technology underscores the potential and critical need for satellite-based platforms capable of profiling the ocean's interior with comparable resolution and depth penetration. Our work not only demonstrates the feasibility but also establishes the scientific necessity for next-generation of spaceborne ocean lidars. By validating the transformative potential of blue-light profiling, we have effectively de-risked and defined the core scientific requirements for future multi-billion dollar missions like CALIGOLA[62] and Guanlan[51], paving the way for a global, continuous monitoring of the ocean's interior. Such missions would revolutionize our ability to globally map phytoplankton vertical structures, quantify carbon export, and understand ocean–climate feedbacks on a planetary scale, thereby building upon the foundational insights provided by airborne systems and ushering in the next era of global ocean observation[15,16].

Methods

High-energy, spectrally-narrowed blue laser source (HEBLS)

Generating a blue laser with the high energy, stability, and spectral purity required for deep-ocean profiling was a key engineering challenge. Our solution is a custom-designed, versatile laser system capable of producing both blue (486 nm) and green (532 nm) pulses. The High-Energy Blue Laser Source (HEBLS) at its core employs a sophisticated three-module architecture to achieve its breakthrough performance (Fig. 5).

1. **The Foundation: A Stable, High-Power Fundamental Laser (1064 nm MOPA)**. The process begins by creating a high-quality, high-energy infrared laser beam at 1064 nm to act as the system's workhorse. We employed a Master Oscillator Power-Amplifier (MOPA) configuration. The Master Oscillator is an electro-optically Q-switched laser designed for stability and precision. It is double-end-pumped by two 808 nm fiber-coupled, quasicontinuous-wave (QCW) laser diodes, which operate at a 100 Hz repetition rate with a 230 μs pulse width. The gain medium is a diffusion-bonded Nd:YAG rod with undoped YAG end caps to reduce thermal effects at the crystal faces; it is wrapped in indium foil and mounted on a conductive-cooled copper heat sink for thermal management. A KD*P Pockels Cell (Gooch & Housego, Impact 8), paired with a Brewster polarizer and a quarter waveplate, serves as the high-speed electro-optical Q-switch. These components are arranged in a compact U-folding resonator design. The output from the oscillator is protected from back-reflections by a high damage threshold isolator before being directed to the power amplifier. This amplifier is a double-pass, side-pumped module utilizing 35 vertical-cavity surface-emitting laser (VCSEL) chips as the pump source. This choice is critical for airborne applications, as VCSELs offer superior thermal stability (wavelength emission drift of 0.07 nm K^{-1}) compared with traditional laser diodes (0.3 nm K^{-1}). The Nd:YAG crystal rod is pumped from five directions for uniform gain. The input signal laser is amplified in a double-pass configuration guided by a quarter waveplate and a polarization beam splitter (PBS). This MOPA design achieves a final 1064 *nm* pulse energy of ~90 mJ with an extraction efficiency of 10%, and crucially, the output energy remains stable across an environmental temperature range of 20–35 °C.
2. **The Engine: An Efficient UV Pump Source (355 nm THG)**. The high-energy 1064 nm infrared beam is converted into a 355 nm ultraviolet (UV) beam to act as the direct energy source, or "pump," for the blue laser OPO. This frequency conversion is achieved through a two-step process within the Third-Harmonic Generation (THG) module. It utilizes two Lithium Triborate (LBO) crystals, each with dimensions of 10 mm × 10 mm × 15 mm. First, a type-I phase-

(a) Structural diagram of a high-energy blue–green dual-wavelength laser

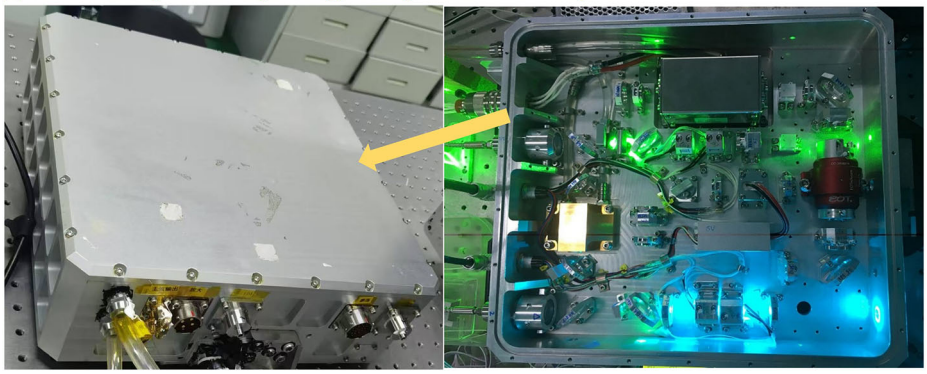

(b) Three functional modules of the dual-wavelength lidar

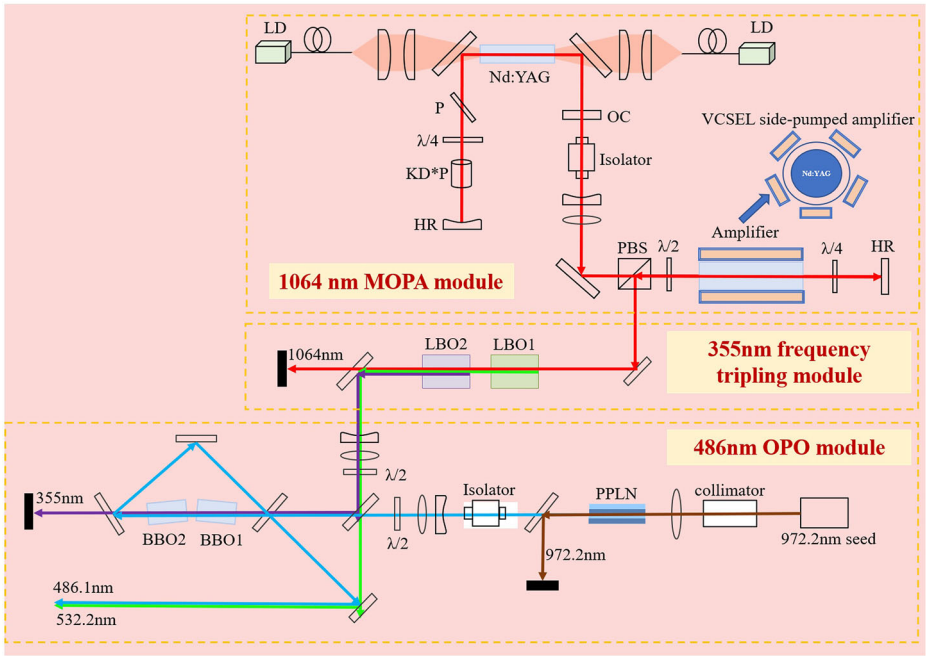

Fig. 5 | High-energy blue–green laser source. a The packaged dual-wavelength laser instrument engineered for robust airborne operation. **b** Detailed optical schematic of the HEBLS architecture, showing its three main functional modules. The system is designed to first create a stable, high-energy 1064 nm MOPA beam, which then pumps a 355 nm frequency tripling module. The resulting UV light finally drives the seeded 486 nm OPO module to generate the spectrally pure blue laser pulses essential for deep-ocean sensing.

matched LBO crystal performs frequency-doubling of the fundamental 1064 nm beam. Then, a second, type-II phase-matched LBO crystal mixes this resulting beam with the residual fundamental beam to generate the final 355 nm UV output. To ensure stable and efficient nonlinear phase-matching, both LBO crystals are actively temperature-controlled with an accuracy of ±0.1 °C, providing a consistent high-power UV pump for the subsequent OPO stage.

3. **The Breakthrough: Spectrally-Locked Blue Laser Generation (486 nm OPO with Seed Injection)**. The final and most innovative step is the conversion of the 35 mJ, 355 nm UV pump laser into the desired 486 nm blue light. This is accomplished using a single-resonance Optical Parametric Oscillator (OPO) with a three-mirror ring cavity design. The cavity mirrors are coated to achieve high transmittance for both the 355 nm pump and the 1313 nm idler laser, whereas the output coupling mirror has 30% transmittance for the 486 nm signal laser, and the other two mirrors are highly reflective at 486 nm.

The parametric gain medium consists of two 8 mm × 8 mm × 20 mm, type-I phase-matched β-BBO crystals. To maximize the conversion efficiency, the two crystals are placed cross-symmetrically relative to the pump light axis to passively compensate for the beam "walk-off" effect. Fine angular adjustment and precise temperature control of the crystals are used to ensure stable phase matching.

The key innovation for achieving the required narrow and stable linewidth is the implementation of a seed injection technique. A continuous-wave, single-longitudinal-mode seed laser at precisely 486.1 nm—itself generated by frequency-doubling a 972.2 nm Distributed Feedback laser with a periodically poled lithium niobate crystal—is injected into the OPO cavity. This "seed" forces the OPO to operate only at this exact wavelength and to adopt its narrow spectral characteristics.

The effect of seed injection is significant (Supplementary Fig. S3). Without the seed, the OPO produces a laser output with a central wavelength of ~486.1 nm but with a relatively broad 3 dB spectral width of ~0.13 nm. While this is already narrower than the receiver's optical bandwidth (0.44 nm), seed injection narrows the spectrum significantly, reaching the resolution limit of our optical spectrum analyzer (Yokogawa, AQ6373B) and precisely matching the H-β Fraunhofer line (~0.1 nm). This spectral locking is crucial for scientific applications, as it allows the receiver's filters to effectively reject broadband solar background noise.

With a 35 mJ pump energy, this seeded OPO module reliably generates 7 mJ blue laser pulses with a pulse width of ~8 ns, corresponding to a parametric conversion efficiency of 20%. The residual green laser energy after the frequency conversion process is ~6.2 mJ with an 8 ns pulse width.

In summary, the architecture of the HEBLS—integrating a 1064 nm MOPA, a 355 nm frequency-tripling module, and a seeded 486 nm OPO—is engineered to deliver the high-energy, narrow-linewidth blue and green laser pulses that are essential for deep ocean profiling.

A hybrid detection system to conquer extreme signal dynamics

A second challenge in oceanic lidar is managing the returned signal, which presents two distinct problems: an enormous dynamic range and intense sea-surface reflections. We solved this with an integrated detection system combining two key technologies: an Analog/Photon-counting Composite Photoelectric Detection (APCD) module to handle the dynamic range, and an Adaptive Dual-Gain sea surface glint rejection Detection (DGD) strategy to nullify surface reflections.

The APCD hardware solution. The system is designed around a single photomultiplier tube (PMT) whose output is split and processed by two parallel electronic pathways, each optimized for a different part of the signal (Supplementary Fig. S4).

- **The Low-Gain Analog Path** is designed to faithfully record intensely bright, near-surface echoes without saturation. It uses a low-gain amplifier to process the strong current into a continuous voltage waveform, which is captured by a high-speed analog-to-digital converter (ADC).
- **The High-Gain Photon-Counting Path** is optimized for maximum sensitivity to faint, single-photon-level returns from deep water. A high-gain amplifier boosts these weak photoelectron pulses, which are then identified and counted as discrete photon events by a specialized multithreshold high-speed comparator.

APCD software solution. The core innovation lies in our three-step digital processing workflow, which seamlessly reconstructs a single, high-fidelity profile from two disparate data streams (Supplementary Fig. S5):

1. **Photon Event Classification:** The process begins by accurately classifying the raw high-gain signal. A software algorithm distinguishes discrete single-photon events from continuous multiphoton signals, while a precise single-photon calibration value is determined through statistical analysis of voltage histograms.
2. **Signal Photonization:** To ensure that the two data streams are compatible, the continuous voltage waveform from the low-gain analog path is quantitatively converted into an equivalent photon number waveform. This conversion uses a precise coefficient derived from the single-photon calibration value.
3. **Seamless Waveform Splicing:** Finally, the high-gain (weak, deep signals) and the photonized low-gain (strong, shallow signals) waveforms are merged into a single continuous profile. A correction coefficient, derived from the system's known field-of-view (FOV) response, is applied to ensure perfect alignment in the overlapping data region. The resulting composite waveform is then corrected for any residual detector after pulse effects, yielding the complete, high-fidelity echo profile with 1 *ns* resolution that is ready for scientific inversion.

This sophisticated APCD process is complemented by the DGD strategy, which uses an adaptive gain and thresholding algorithm to specifically identify and reject intense, brief flashes from the sea surface. The technology combines optical splitting, optical spatial filtering, and adaptive detector gain control. The path with a lower splitting ratio serves as the shallow-water channel, where the detector gain is automatically adjusted on the basis of the intensity of the sea surface echo to ensure the integrity of the sea surface and shallow-water signals. The path with a higher splitting ratio serves as the deep-water channel; an optical spatial filter is added to this channel to suppress interference from strong sea surface signals, and the detector is set to a high gain to enable the detection of weak photon echo signals from deep water. This preserves the integrity of the crucial data from just below the surface downward, completing our solution to the signal dynamics challenge.

This advanced APCD, coupled with DGD, provides an unparalleled capability for accurately resolving the full vertical distribution of chlorophyll-*a* from the ocean surface to significant depths, even in the presence of strong surface reflections.

SNR method for lidar detection performance evaluation

To quantitatively assess the detection capability of our oceanic lidar systems and facilitate a rigorous comparison of the penetration performance between blue and green lidar wavelengths, we rigorously calculated the signal-to-noise ratio (SNR) of the returned lidar signal. The SNR is fundamentally defined as the ratio of the received signal power from the water column to the total noise power and is expressed as:

$$SNR = \frac{P_{water}}{P_{bg} + P_d} \quad (1)$$

Here, P_{water} represents the lidar return signal power at a given depth z. P_{bg} denotes the background noise, which primarily originates from solar radiation and scattered environmental light. This background noise is highly variable and influenced by factors such as solar angle, sea surface reflectance, time of day, and atmospheric conditions (e.g., clouds and aerosols), all of which can significantly reduce the dynamic range of detectable signals, especially during daytime observations. The background noise P_{bg} is estimated by calculating the mean value of the final 100 samples in each lidar signal, and this value is systematically subtracted from the entire echo signal[22,63]. P_d corresponds to the dark count noise, an inherent characteristic of the photomultiplier tube (PMT) when operating in photon-counting mode. The P_d was characterized and determined in the laboratory prior to the campaigns by measuring the instrument's intrinsic noise with the laser turned off. These dark counts typically arise from thermally generated electrons, internal circuit noise, or intrinsic material excitations within the PMT, follow a Poisson distribution, and can contribute substantially to the total noise under low-light conditions.

To ensure the reliability and physical interpretability of subsurface optical property retrievals, we define a critical SNR threshold of 4 to delineate the laser's maximum effective penetration depth. Below this threshold, the lidar signal becomes increasingly contaminated by background noise and detector dark counts, leading to amplified uncertainties and compromising the physical interpretability of the inversion outputs. To mitigate these effects and ensure robust retrievals, the lidar inversion algorithm, which is used for deriving optical properties, is applied only to depths where the SNR ≥ 4. This restriction ensures a stable reference depth and significantly minimizes error propagation throughout the inversion process.

Lidar inversion model and validation

The direct measured and core data products generated by our system are high-resolution vertical profiles of Kd and bbp. As fundamental optical properties, Kd and bbp have direct applications in many ecological and biogeochemical models. Retrieving accurate vertical profiles of optical properties and chlorophyll-*a* from lidar signals in optically complex and heterogeneous ocean environments presents challenges. To address this, we developed a hybrid iterative lidar inversion model[21,22,64–66] specifically designed for robust chlorophyll-*a* profiling. The lidar system directly measures the return signal, from which we first retrieve physical optical properties (like the diffuse attenuation coefficient, Kd, and the particulate backscattering coefficient, bbp). These physical parameters are then used as inputs to a physically-constrained machine learning model (XGBoost) to estimate chlorophyll-a concentration. The complete computational workflow of this study, which encompasses data processing, optical property retrieval, and chlorophyll-*a* inversion, is illustrated in Supplementary Fig. S6 and comprises five major steps:

Step 1: Waveform stitching

The initial critical step involves processing the raw lidar return signals, which span an extremely large dynamic range. This begins with the precise merging of voltage waveforms from the photomultiplier tube (PMT) corresponding to single-photon (weak, deep signals) and multiphoton (strong, near-surface signals) detection modes. Following this sophisticated merging

process, dedicated waveform correction procedures are applied to reconstruct complete, continuous, and physically meaningful signal profiles[67,68], as detailed in the "APCD + DGD" section.

Step 2: Data preprocessing

As a pivotal step influencing the accuracy of subsequent profile inversion, data preprocessing entails a series of rigorous correction procedures applied to the merged raw waveforms. These include:

- Background Bias Correction: Removal of environmental light and dark count contributions.
- Precise Water Surface Identification and Calibration: Accurate determination of the sea surface reference point, which is critical for range calculation.
- Range Correction: Normalization of signal intensity for geometric spreading effects.

The preprocessed profiles are then georeferenced via an integrated position and orientation system (POS) to assign precise latitude and longitude coordinates. Gain calibration is applied via onboard calibration data. A comprehensive denoising protocol is subsequently implemented, incorporating temporal averaging, spatial smoothing, frequency-domain filtering, and localized window or regression smoothing techniques, all of which are optimized to significantly enhance signal quality across the entire water column.

Step 3: Iterative Hybrid Multiple Scattering Correction (IHMSC) model development

To accurately retrieve the vertical distributions of the diffuse attenuation coefficient (K_d) and the particulate backscattering coefficient (b_{bp}), we introduce a Iterative Hybrid Multiple Scattering Correction (IHMSC) method, hereafter referred to as the "Deep-Ocean Lidar Inversion" (DOLI) framework. This approach builds upon widely adopted frameworks, such as the Klett method and perturbation techniques[22], but crucially incorporates dynamic optimization over two key parameters: the logarithmic backscatter-to-attenuation ratio (k) and the lidar ratio (R). By iteratively exploring the solution space within physically plausible bounds, the model robustly identifies the optimal values of K_{lidar} and β. Unlike traditional empirical models, which often fail to account for local hydrological and atmospheric variability, our IHMSC approach explicitly incorporates site-specific and climate-dependent factors that significantly affect lidar signal behavior, which is particularly crucial for accurate reconstruction of deep vertical profiles, extending to depths of up to 100 m. Through this iterative framework, the model substantially improves the retrieval accuracy of subsurface optical properties under diverse water conditions.

The fundamental lidar equation is expressed as:

$$P(z) = C\frac{\beta_\pi(z)}{(nH+z)^2}\cdot exp\left(-2\int_0^z K_{lidar}(z)dz\right) \tag{2}$$

where $P(z)$ is the received power at depth z, C is the lidar system constant, K_{lidar} is the lidar attenuation coefficient, β_π is the volume scattering function at 180°, n is the refractive index of water, and H is the airborne lidar altitude.

To linearize this equation, we multiply both sides by $(nH+z)^2$ and take the logarithm, yielding the range-corrected signal $S(z)$:

$$S(z) = ln(P(z)\cdot(nH+z)^2) = ln(C\cdot\beta(z)) - 2\int_0^z K_{lidar}(z)dz \tag{3}$$

Under the Klett inversion framework, we adopt the commonly used power law assumption:

$$\beta(z) = C\cdot K_{lidar}^k(z) \tag{4}$$

where C is a constant and where k denotes the logarithmic backscatter-to-attenuation ratio, which is influenced by the laser wavelength and water optical properties. To determine the optimal k, we perform iterative computations across the range 0.6–1.3 with a step size of 0.1. For each candidate k, the corresponding attenuation coefficient profile $K_{lidar}(z)$ is calculated via the backward integration Klett solution:

$$K_{lidar}(z) = \frac{exp\left[\frac{S(z)-S_m}{k}\right]}{K_{lidar}(z_m)^{-1} + \frac{2}{k}\int_z^{z_m}\exp\left[\frac{S(z)-S_m}{k}\right]dz} \tag{5}$$

where z_m is the reference depth, S_m is the lidar power at z_m, and $K_{lidar}(z_m)$ is the lidar attenuation coefficient at the reference depth, derived via the slope method:

$$K_{lidar}(z_m) = -\frac{1}{2}\frac{dS_m}{dz_m} \tag{6}$$

Unlike conventional perturbation-based inversion methods that rely on static parameterization, our IHMSC incorporates an additional iterative procedure to estimate the backscatter coefficient $\beta(z)$ more robustly. We first compute a reference backscatter coefficient $\beta_{pr}(z)$ via a perturbation method. The initial lidar ratio at the sea surface R_0 is then estimated. An iterative adjustment of R is conducted within a range of ±20% around R_0. The value of $\beta(z)$ that minimizes the deviation from $\beta_{pr}(z)$ is selected as the final inversion output. The calculation formulas are as follows:

$$\beta_{pr}(z) = \frac{S(z)}{S_h(z)}\beta_{pr}(0) \tag{7}$$

$$S_h(z) = \ln(C\beta_{pr}^{non}) - 2K_{lidar}^{non} \tag{8}$$

$$\beta_{pr}(0) = \frac{exp(S(0))}{C} \tag{9}$$

$$R_0 = \frac{K_{lidar}(0) - K_w}{\beta_{pr}(0) - \beta_w} \tag{10}$$

where $K_{lidar}(0)$ and $\beta_{pr}(0)$ denote the lidar attenuation coefficient and the backscatter coefficient at the sea surface, respectively; K_{lidar}^{non} and β_{pr}^{non} are the mean nonvarying parts for K_{lidar} and β_{pr}, respectively, obtained from linear fitting of $S_h(z)$ for $S(z)$; and R_0 is the lidar ratio calculated at the sea surface. On this basis, an iterative approach is employed to estimate the backscatter coefficient for various lidar ratios. The estimated results are then compared to β_{pr}, and the lidar ratio that minimizes the discrepancy is selected as the inverted attenuation coefficient. Finally, the retrieved backscatter coefficient (β) is converted into the particulate backscattering coefficient (bbp) via:

$$bbp(z) = 2\pi\chi\left(\beta(z) - 0.19\times10^{-4}\right) \tag{11}$$

where χ is a conversion factor relating β to bbp. In this study, we assume that χ=1.06 [69–71].

To address the inherent deviation between the lidar-derived attenuation coefficient (K_{lidar}) and the true diffuse attenuation coefficient (K_d) caused by complex multiple scattering effects, we propose a semianalytical radiative transfer model integrated with machine learning[64,72–74]. This model fundamentally builds upon radiative transfer theory, dynamically coupling key physical parameters of the lidar system—including the field of view (FOV), laser divergence angle (DIV), detection height (H), and laser beam nadir angle (θ)—with the intrinsic aquatic optical properties (absorption coefficient a, scattering coefficient b, and backscattering coefficient b_b). This robust coupling yields a dynamic mathematical representation of the light–water interaction process, enabling adaptive and quantitative characterization of laser signal propagation in heterogeneous waters. A data-driven scheme is constructed in which K_{lidar} and lidar system parameters are used as inputs to predict K_d, leveraging K_d values derived from ocean color

products or in situ measurements as training references:

$$K_d = f(K_{lidar}, FOV, DIV, H, \theta, a, b, b_b) \quad (12)$$

where a, b, and b_b are the absorption, scattering, and backscattering coefficients, respectively, obtained from ocean color data or in situ measurements. The implementation of an optimized gradient boosting algorithm accelerates decision tree training while preserving transparency in the model's physical basis. Importantly, this hybrid approach offers a computationally efficient alternative to conventional Monte Carlo simulations, overcoming their bottlenecks while maintaining accurate representation of complex scattering regimes. A sensitivity-optimized parameterization scheme ensures robust coupling between lidar system specifications and aquatic optical properties (further details in our previous studies). This versatile framework facilitates both forward performance modeling and inversion algorithm development for airborne lidar systems, demonstrating particular strength in optically complex coastal–offshore transitional zones where conventional retrieval methods often fail.

Step 4: Physics-guided chlorophyll profile retrieval with XGBoost

The final step in our workflow is the retrieval of chlorophyll-*a* vertical profiles from the lidar-derived optical properties. While traditional empirical algorithms exist, they often fail to capture complex, nonlinear bio-optical relationships that vary across different water types. To overcome this, we employ a physics-guided machine learning approach with an XGBoost model. Unlike traditional non-linear curve fitting, which requires a presupposed functional form, XGBoost, as a gradient boosting decision tree algorithm, can automatically learn and capture highly complex, non-linear, and interactive relationships among multi-dimensional input features. This makes it a more powerful and robust tool for tackling complex bio-optical problems.

Crucially, this model is not a "black box." Its predictive power is fundamentally anchored in physical measurements. The input features for the model are the vertical profiles of the diffuse attenuation coefficient (K_d) and the particulate backscattering coefficient (*bbp*), which are retrieved via our rigorous, physics-based DOLI framework (Step 3). While Kd and bbp are derived from the same lidar signal and are therefore not statistically independent, they represent distinct physical properties of the water column. Using them jointly provides a more robust physical constraint on the bio-optical model than using either parameter alone. This ensures that the model learns from inputs with clear physical significance rather than from unconstrained correlations. Here, the derived K_d and *bbp* profiles serve as input features, whereas the measured chlorophyll profiles act as target variables. The trained XGBoost model successfully reconstructs chlorophyll vertical distributions from three independent lidar datasets. By rigorously modeling complex interactions among these variables, XGBoost significantly enhances both the robustness of retrievals and the adaptability of the method to heterogeneous marine environments.

Step 5: Validation

To rigorously evaluate the accuracy and reliability of the lidar-derived vertical chlorophyll-*a* inversion products, a comprehensive comparison between our model results and independent in situ measured data was conducted. At stations S1-S3, we used an RBRconcerto^3 C.T.D profiler equipped with an RBR *solo*^{3} FLR fluorometer to synchronously collect in situ vertical profiles of chlorophyll-a concentration. The raw fluorescence data were converted to chlorophyll-a concentration using a linear calibration factor, which was derived from laboratory fluorescence measurements of water samples collected at various depths at each station. Furthermore, we corrected for the non-photochemical quenching (NPQ) effect in the near-surface layer for profiles collected during the daytime, following standard procedures[75]. The evaluation relies on four widely accepted statistical metrics, used to assess the consistency and agreement between the datasets:

1. Bias: Measures the systematic difference between the model-derived and in situ measured values, indicating potential overestimation or underestimation.

$$Bias = \frac{\sum_{i=1}^{n}(x_i - y_i)}{n} \quad (13)$$

where x_i represents the lidar-derived value, y_i represents the in situ measured value, and n is the number of data points.

2. Pearson Correlation Coefficient (R): This coefficient reflects the linear relationship between two datasets. R ranges from −1 to 1; values closer to 1 or −1 indicate a stronger positive or negative linear correlation, respectively, whereas values near 0 suggest no linear correlation. In our case, a higher R value implies a better match in the patterns of vertical chlorophyll-*a* distribution between the model and in situ data.

$$R = \frac{\sum_{i=1}^{n}(x_i - \bar{x})(y_i - \bar{y})}{\sqrt{\sum_{i=1}^{n}(x_i - \bar{x})^2 \sum_{i=1}^{n}(y_i - \bar{y})^2}} \quad (14)$$

where $\bar{x}$ and $\bar{y}$ are the mean values of the lidar-derived and in situ data, respectively.

3. Root Mean Square Error (RMSE): This represents the standard deviation of the residuals (differences between the model and measured values). A lower RMSE signifies that the model-derived values are closer to the in situ measurements on average, indicating higher accuracy.

$$RMSE = \sqrt{\frac{\sum_{i=1}^{n}(x_i - y_i)^2}{n-1}} \quad (15)$$

4. Mean Absolute Percentage Difference (MAPD): This expresses the average magnitude of the differences relative to the measured values, providing a percentage-based measure of accuracy. A smaller MAPD indicates that the model-derived chlorophyll-*a* values are more accurate than the in situ measurements are.

$$MAPD = \frac{\sum_{i=1}^{n}\left|\frac{x_i - y_i}{y_i} \times 100\%\right|}{n} \quad (16)$$

Data availability

The processed data generated in this study, including the source data underlying the figures, have been deposited in the Zenodo database under the identifier https://doi.org/10.5281/zenodo.17577166.

Code availability

The code used for all data processing, analysis, and figure generation in this study is publicly available deposited in the Zenodo database under the identifier https://doi.org/10.5281/zenodo.17577166.

Received: 14 August 2025; Accepted: 13 November 2025;
Published online: 27 November 2025

References

1. Falkowski, P. Ocean science: the power of plankton. *Nature* **483**, S17–S20 (2012).
2. Westberry, T., Behrenfeld, M., Siegel, D. & Boss, E. Carbon-based primary productivity modeling with vertically resolved photoacclimation. *Glob. Biogeochem. Cycles* **22**, https://doi.org/10.1029/2007GB003078 (2008).
3. Field, C. B., Behrenfeld, M. J., Randerson, J. T. & Falkowski, P. Primary production of the biosphere: integrating terrestrial and oceanic components. *Science* **281**, 237–240 (1998).
4. Cornec, M. et al. Deep Chlorophyll maxima in the global ocean: occurrences, drivers and characteristics. *Glob. Biogeochem. Cycles* **35**, e2020GB006759 (2021).

5. Cullen & John, J. Subsurface chlorophyll maximum layers: enduring enigma or mystery solved?. *Annu. Rev. Mar. Sci.* **7**, 207 (2015).
6. Durham, W. M. & Stocker, R. Thin phytoplankton layers: characteristics, mechanisms, and consequences. *Annu. Rev. Mar. Sci.* **4**, 177–207 (2012).
7. Stammer, D. et al. Ocean climate observing requirements in support of climate research and climate information. *Front. Mar. Sci.* **6**, 2019 (2019).
8. Wirtz, K., Smith, S. L., Mathis, M. & Taucher, J. Vertically migrating phytoplankton fuel high oceanic primary production. *Nat. Clim. Chang.* **12**, 750–756 (2022).
9. Holly, V. et al. Light-dependent grazing can drive formation and deepening of deep chlorophyll maxima. *Nat. Commun.* **10**, 1978 (2019).
10. Chavez, F. P., Messié, M. & Pennington, J. T. Marine primary production in relation to climate variability and change. *Annu. Rev. Mar. Sci.* **3**, 227–260 (2011).
11. Anderson, R. F. GEOTRACES: accelerating research on the marine biogeochemical cycles of trace elements and their isotopes. *Annu. Rev. Mar. Sci.* **12**, 49–85 (2020).
12. Pierella Karlusich, J. J., Ibarbalz, F. M. & Bowler, C. Phytoplankton in the Tara ocean. *Annu Rev. Mar. Sci.* **12**, 233–265 (2020).
13. Chai, F. et al. Monitoring ocean biogeochemistry with autonomous platforms. *Nat. Rev. Earth Environ.* **1**, 315–326 (2020).
14. McClain, C. R. A decade of satellite ocean color observations. *Annu. Rev. Mar. Sci.* **1**, 19–42 (2009).
15. Hostetler, C. A., Behrenfeld, M. J., Hu, Y., Hair, J. W. & Schulien, J. A. Spaceborne lidar in the study of marine systems. *Annu. Rev. Mar. Sci.* **10**, 121–147 (2018).
16. Jamet, C. et al. Going beyond standard ocean color observations: lidar and polarimetry. *Front. Mar. Sci.* **6**, 251 (2019).
17. Johnson, K. S. et al. Observing biogeochemical cycles at global scales with profiling floats and gliders: prospects for a global array. *Oceanography* **22**, 216–225 (2009).
18. Moore, T. S. et al. Vertical distributions of blooming cyanobacteria populations in a freshwater lake from LIDAR observations. *Remote Sens. Environ.* **225**, 347–367 (2019).
19. Churnside, J. H. & Marchbanks, R. D. Subsurface plankton layers in the Arctic Ocean. *Geophys. Res. Lett.* **42**, 4896–4902 (2015).
20. Churnside, J. H. & Donaghay, P. L. Thin scattering layers observed by airborne lidar. *ICES J. Mar. Sci.* **66**, 778–789 (2009).
21. Chen, P., Jamet, C. & Liu, D. LiDAR remote sensing for vertical distribution of seawater optical properties and chlorophyll-a from the East China Sea to the South China Sea. *IEEE Trans. Geosci. Remote Sens.* **60**, 1–21 (2022).
22. Chen, P. et al. Vertical distribution of subsurface phytoplankton layer in South China Sea using airborne lidar. *Remote Sens. Environ.* **263**, 112567 (2021).
23. Wright, C. W., Hoge, F. E., Swift, R. N., Yungel, J. K. & Schirtzinger, C. R. Next-generation NASA airborne oceanographic lidar system. *Appl. Opt.* **40**, 336–342 (2001).
24. Hoge, F. E., Vodacek, A. & Blough, N. V. Inherent optical properties of the ocean: retrieval of the absorption coefficient of chromophoric dissolved organic matter from fluorescence measurements. *Limnol. Oceanogr.* **38**, 1394–1402 (1993).
25. Hoge, F. E. et al. Airborne lidar detection of subsurface oceanic scattering layers. *Appl. Opt.* **27**, 3969–3977 (1988).
26. Vasilkov, A. P. et al. Airborne polarized lidar detection of scattering layers in the ocean. *Appl. Opt.* **40**, 4353–4364 (2001).
27. Hoge, F. E. Validation of satellite-retrieved oceanic inherent optical properties: proposed two-color elastic backscatter lidar and retrieval theory. *Appl. Opt.* **42**, 7197–7201 (2003).
28. Behrenfeld, M. J. et al. Global satellite-observed daily vertical migrations of ocean animals. *Nature* **576**, 257–261 (2019).
29. Behrenfeld, M. J. et al. Annual boom-bust cycles of polar phytoplankton biomass revealed by space-based lidar. *Nat. Geosci.* **10**, 118–122 (2016).
30. Zhang, Z. et al. Combining deep learning with physical parameters in POC and PIC inversion from spaceborne lidar CALIOP. *ISPRS J. Photogramm. Remote Sens.* **212**, 193–211 (2024).
31. Zhang, Z. et al. Retrieving bbp and POC from CALIOP: a deep neural network approach. *Remote Sens. Environ.* **287**, 113482 (2023).
32. Bogucki, D. J. & Spiers, G. What percentage of the oceanic mixed layer is accessible to marine Lidar? Global and the Gulf of Mexico prospective. *Opt. Express* **21**, 23997–24014 (2013).
33. Behrenfeld, M., Hu, Y., Bisson, K., Lu, X. & Westberry, T. Retrieval of ocean optical and plankton properties with the satellite Cloud-Aerosol Lidar with Orthogonal Polarization (CALIOP) sensor: background, data processing, and validation status. *Remote Sens. Environ.* **281**, 113235 (2022).
34. Churnside, J. H. & Shaw, J. A. Lidar remote sensing of the aquatic environment: invited. *Appl. Opt.* **59**, C92–C99 (2020).
35. Thomalla, S. J., Nicholson, S.-A., Ryan-Keogh, T. J. & Smith, M. E. Widespread changes in Southern Ocean phytoplankton blooms linked to climate drivers. *Nat. Clim. Change* **13**, 975–984 (2023).
36. Ardyna, M. & Arrigo, K. R. Phytoplankton dynamics in a changing Arctic Ocean. *Nat. Clim. Change* **10**, 892–903 (2020).
37. Behrenfeld, M. J., Boss, E., Siegel, D. A. & Shea, D. M. Carbon-based ocean productivity and phytoplankton physiology from space. *Glob. Biogeochem. Cycles* **19**, https://doi.org/10.1029/2004GB002299 (2005).
38. Kitchen, J. C. & Zaneveld, J. R. V. On the noncorrelation of the vertical structure of light scattering and chlorophyll α in case I waters. *J. Geophys. Res. Oceans* **95**, 20237–20246 (1990).
39. Blooms, M.-O. P. Eddy/wind interactions stimulate extraordinary. *Deep-Sea Res.* **1**, 829 (2003).
40. Qiu, B., Chen, S., Klein, P., Sasaki, H. & Sasai, Y. Seasonal mesoscale and submesoscale eddy variability along the North Pacific Subtropical Countercurrent. *J. Phys. Oceanogr.* **44**, 3079–3098 (2014).
41. Qiu, B. & Chen, S. Interannual variability of the North Pacific Subtropical Countercurrent and its associated mesoscale eddy field. *J. Phys. Oceanogr.* **40**, 213–225 (2010).
42. Lévy, M., Ferrari, R., Franks, P. J., Martin, A. P. & Rivière, P. Bringing physics to life at the submesoscale. *Geophys. Res. Lett.* **39**, https://doi.org/10.1029/2012GL052756 (2012).
43. Mahadevan, A. The impact of submesoscale physics on primary productivity of plankton. *Annu. Rev. Mar. Sci.* **8**, 161–184 (2016).
44. d'Ovidio, F., De Monte, S., Alvain, S., Dandonneau, Y. & Lévy, M. Fluid dynamical niches of phytoplankton types. *Proc. Natl. Acad. Sci.* **107**, 18366–18370 (2010).
45. Schulien, J. A., Behrenfeld, M. J., Hair, J. W., Hostetler, C. A. & Twardowski, M. S. Vertically- resolved phytoplankton carbon and net primary production from a high spectral resolution lidar. *Opt. Express* **25**, 13577–13587 (2017).
46. Wang, S. et al. A more quiescent deep ocean under global warming. *Nat. Clim. Chang.* **14**, 961–967 (2024).
47. Ratnarajah, L. et al. Monitoring and modelling marine zooplankton in a changing climate. *Nat. Commun.* **14**, 564 (2023).
48. Viljoen, J. J., Sun, X. & Brewin, R. J. W. Climate variability shifts the vertical structure of phytoplankton in the Sargasso Sea. *Nat. Clim. Chang.* **14**, 1292–1298 (2024).
49. Schulien, J. A. et al. Shifts in phytoplankton community structure across an anticyclonic eddy revealed from high spectral resolution lidar scattering measurements. *Front. Mar. Sci.* **7**, 2020 (2020).
50. Wang, W.-L. et al. Biological carbon pump estimate based on multidecadal hydrographic data. *Nature* **624**, 579–585 (2023).
51. Chen, G., Tang, J., Zhao, C., Wu, S. & Wu, L. Concept design of the "Guanlan" science mission: China's novel contribution to space oceanography. *Front. Mar. Sci.* **6**, https://doi.org/10.3389/fmars.2019.00194 (2019).
52. Uitz, J., Claustre, H., Morel, A. & Hooker, S. B. Vertical distribution of phytoplankton communities in open ocean: an assessment based on surface chlorophyll. *J. Geophys. Res.* **111**, C08005 (2006).

53. Doney, S. C. et al. Climate change impacts on marine ecosystems. *Annu. Rev. Mar. Sci.* **4**, 11–37 (2012).
54. Ferreira, A. et al. Climate change is associated with higher phytoplankton biomass and longer blooms in the West Antarctic Peninsula. *Nat. Commun.* **15**, 6536 (2024).
55. Mackay, N., Watson, A. J., Suntharalingam, P., Chen, Z. & Landschützer, P. Improved winter data coverage of the Southern Ocean CO2 sink from extrapolation of summertime observations. *Commun. Earth Environ.* **3**, 265 (2022).
56. Brewin, R. J. W. et al. Ocean carbon from space: current status and priorities for the next decade. *Earth Sci. Rev.* **240**, 104386 (2023).
57. Alhassan, Y., Siekmann, I. & Petrovskii, S. Mathematical model of oxygen minimum zones in the vertical distribution of oxygen in the ocean. *Sci. Rep.* **14**, 22248 (2024).
58. Cheung, W. W. L. et al. Projecting global marine biodiversity impacts under climate change scenarios. *Fish Fish.* **10**, 235–251 (2009).
59. Behrenfeld, M. J. et al. Satellite-detected fluorescence reveals global physiology of ocean phytoplankton. *Biogeosciences* **6**, 779–794 (2009).
60. Lam, V. W. Y., Cheung, W. W. L., Reygondeau, G. & Sumaila, U. R. Projected change in global fisheries revenues under climate change. *Sci. Rep.* **6**, 32607 (2016).
61. Henson, S. A., Cael, B. B., Allen, S. R. & Dutkiewicz, S. Future phytoplankton diversity in a changing climate. *Nat. Commun.* **12**, 5372 (2021).
62. Behrenfeld, M. J. et al. Satellite lidar measurements as a critical new global ocean climate record. *Remote Sens.* **15**, 5567 (2023).
63. Li, X., Chen, P., Zhang, Z., Li, Y. & Pan, D. Vertical structure observation from spaceborne lidar ICESat-2 in East China Sea. *Opt. Express* **33**, 2847–2865 (2025).
64. Chen, S., Chen, P., Kong, W., Shu, R. & Pan, D. A Semi-analytical method for ocean LiDAR radiative transfer considering inelastic and polarized scattering. *IEEE Trans. Geosci. Remote Sens.* 63, 1–16 (2025).
65. Zhang, S. & Chen, P. Subsurface phytoplankton vertical structure from lidar observation during SCS summer monsoon onset. *Opt. Express* **30**, 17665–17679 (2022).
66. Chen, P. Subsurface phytoplankton vertical structure observations using offshore fixed platform-based lidar in the Bohai Sea for offshore responses to Typhoon Bavi. *Opt. Express* **30**, 20614–20628 (2022).
67. Collister, B. L., Zimmerman, R. C., Hill, V. J., Sukenik, C. I. & Balch, W. M. Polarized lidar and ocean particles: insights from a mesoscale coccolithophore bloom. *Appl. Opt.* **59**, 4650–4662 (2020).
68. Collister, B. L., Zimmerman, R. C., Sukenik, C. I., Hill, V. J. & Balch, W. M. Remote sensing of optical characteristics and particle distributions of the upper ocean using shipboard lidar. *Remote Sens. Environ.* **215**, 85–96 (2018).
69. Zhang, X., Gray, D. J., Huot, Y., You, Y. & Bi, L. Comparison of optically derived particle size distributions: scattering over the full angular range versus diffraction at near forward angles. *Appl. Opt.* **51**, 5085–5099 (2012).
70. Sullivan, J. M. & Twardowski, M. S. Angular shape of the oceanic particulate volume scattering function in the backward direction. *Appl. Opt.* **48**, 6811–6819 (2009).
71. Chami, M., Thirouard, A. & Harmel, T. POLVSM (Polarized Volume Scattering Meter) instrument: an innovative device to measure the directional and polarized scattering properties of hydrosols. *Opt. Express* **22**, 26403–26428 (2014).
72. Chen, S., Chen, P., Kong, W., Shu, R. & Pan, D. SAMC: A novel semi-analytical method for simulating full-polarization LiDAR signals in marine environments. *IEEE Trans. Geosci. Remote Sens.* **63**, 1–16 (2025).
73. Wu, D., Chen, P., Kong, W. & Pan, D. A novel semi-analytical method for modeling polarized oceanic profiling LiDAR multiple scattering signals. *IEEE Trans. Geosci. Remote Sens.* **62**, 1–17 (2024).
74. Chen, P., Jamet, C., Mao, Z. & Pan, D. OLE: a novel oceanic LiDAR emulator. *IEEE Trans. Geosci. Remote Sens.* **59**, 9730–9744 (2021).
75. Xing, X., Briggs, N., Boss, E. & Claustre, H. Improved correction for non-photochemical quenching of in situ chlorophyll fluorescence based on a synchronous irradiance profile. *Opt. Express* **26**, 24734–24751 (2018).

Acknowledgements

This study was supported by the National Natural Science Foundation of China (Grant #42322606; Grant #42276180; Grant #W2521002), the Zhejiang Provincial Natural Science Foundation (Grant #LZ25D060001), and the National Key Research and Development Program of China (Grant #2022YFB3901703; Grant #2022YFB3902603). This research was supported by the International Space Science Institute (ISSI) in Bern and Beijing, through ISSI/ISSI-BJ International Team project 'Toward a 3-D Observation of the Ocean Color: Benefit of Lidar Technique' (ISSI Team project #530; ISSI-BJ Team project #50).

Author contributions

C.P. and Z.Z. conceived the study and prepared the original manuscript. Z.Z., S.Z., and D.P. provided parts of the data. W.C., Y.H., K.S., C.J., P.G., D.D., and X.L. prepared and/or revised the manuscript.

Competing interests

The authors declare no competing interests.

Additional information

Supplementary information The online version contains supplementary material available at https://doi.org/10.1038/s43247-025-03034-1.

Correspondence and requests for materials should be addressed to Chen Peng, Weibiao Chen, Yan He or Kun Shi.

Peer review information *Communications Earth and Environment* thanks Richard Zimmerman and the other, anonymous, reviewer(s) for their contribution to the peer review of this work. Primary Handling Editors: Nadine Schubert and Alice Drinkwater. [A peer review file is available].

Reprints and permissions information is available at http://www.nature.com/reprints

Publisher's note Springer Nature remains neutral with regard to jurisdictional claims in published maps and institutional affiliations.

Open Access This article is licensed under a Creative Commons Attribution-NonCommercial-NoDerivatives 4.0 International License, which permits any non-commercial use, sharing, distribution and reproduction in any medium or format, as long as you give appropriate credit to the original author(s) and the source, provide a link to the Creative Commons licence, and indicate if you modified the licensed material. You do not have permission under this licence to share adapted material derived from this article or parts of it. The images or other third party material in this article are included in the article's Creative Commons licence, unless indicated otherwise in a credit line to the material. If material is not included in the article's Creative Commons licence and your intended use is not permitted by statutory regulation or exceeds the permitted use, you will need to obtain permission directly from the copyright holder. To view a copy of this licence, visit http://creativecommons.org/licenses/by-nc-nd/4.0/.

© The Author(s) 2025